



CuS modified graphite from spent Li-ion batteries towards building high energy Na-ion capacitors *via* solvent-co-intercalation process

Manohar Akshay^a, Shaji Jyothilakshmi^a, Yun-Sung Lee^{b,*}, Vanchiappan Aravindan^{a,*}

^a Department of Chemistry, Indian Institute of Science Education and Research (IISER), Tirupati 517619, India

^b School of Chemical Engineering, Chonnam National University, Gwang-ju 61186, Republic of Korea

ARTICLE INFO

Keywords:

Na-ion Capacitors
Anode
Graphite
Solvent-co-intercalation
recycling spent LIB

ABSTRACT

Sodium-ion capacitors (NICs) are one of the most modern hybrid energy storage devices, and they involve two different energy storage mechanisms (faradaic and non-faradaic). The NICs are bridging the gap between the Na-ion batteries and the capacitors with enhanced power and energy densities. This work explores a new combination electrode material, *i.e.*, recovered graphite (RG) decorated with copper sulphide (CuS, CS) as the anode for the NIC application, in which graphite undergoes the solvent-co-intercalation process, and CuS adopts the conversion reaction. We also report the possibility of efficient direct recovery of the anode of dead/spent Li-ion batteries and upcycling as a battery-type component for NIC with commercially available activated carbon (AC) as the capacitor-type cathode. First, the Na-storage property is analyzed in the half-cell configuration, where the Na/RG-CS half-cell displayed excellent cyclic stability with a stable specific capacity of 113 mAh g⁻¹ after 500 cycles with >96% coulombic efficiency in ether solutions. With a pre-sodiated form of RG-CS as anode and mass-balanced AC as a cathode, the NIC is fabricated. The NIC displayed a superior energy density of 64.6 Wh kg⁻¹ with ultra-long cyclability for more than 10,000 cycles with >85% capacity retention. The compatibility of the NIC in different environmental conditions is also studied, and the cell renders better performance in all temperature conditions.

1. Introduction

The demand for energy increases exponentially with the increase in the population around the world. Consequently, the exploitation of traditional fossil fuels (still the primary energy source) is approaching its peak. This would eventually increase the concentration of greenhouse gases (CO₂, CH₄, N₂O, etc.) in the atmosphere, thereby leading to global warming and other adverse effects on the environment. This could be mitigated by transitioning from these fossil fuels to clean, environmentally friendly, and renewable energy sources such as wind, solar, tidal, etc. However, these energy sources are intermittent and should be efficiently stored for future needs. Among the different energy storage technologies, the electrochemical methods, particularly batteries and capacitors have gained particular interest because of their efficiency, quick charging, high energy density, long cycle life, and low maintenance [1,2]. Metal-ion batteries (MIBs) and Supercapacitors (SCs) are the two prominent energy storage devices with different kinds of charge storage mechanisms. The former stores energy by redox reactions, whereas the latter utilizes the adsorption/desorption process for energy

storage. The MIBs have high energy density and low self-discharge but lack of power density and extended cycle life. In contrast, SCs have high power density and long cycling life but suffer from poor energy density and high self-discharge. Recently, a new class of devices, the hybrid capacitor, has been introduced. It has the combined properties of both MIBs and SCs and meets the limitations of both devices. The synergic effect of the combination of battery-type and capacitive-type electrodes creates an efficient device with high energy density, power density, cyclability, etc., which is anticipated to bridge the gap between sodium-ion batteries (NIBs) and SC [3–5].

Among the hybrid capacitors, Na-ion capacitors (NICs) are one of the green choice and a better replacement for Li-based energy storage devices [6–9]. The cost-effectiveness and global distribution of sodium make it a suitable candidate for the hybrid capacitor. Hybrid capacitors (Lithium-ion capacitors (LICs)/NICs) have a battery/electrochemical electrode as the anode and a capacitive/electrostatic electrode as the cathode. The energy/power density, rate capability, and overall performance of NIC mainly depend upon the electrochemical behaviour of the anode. On this note, various anodic materials, including

* Corresponding authors.

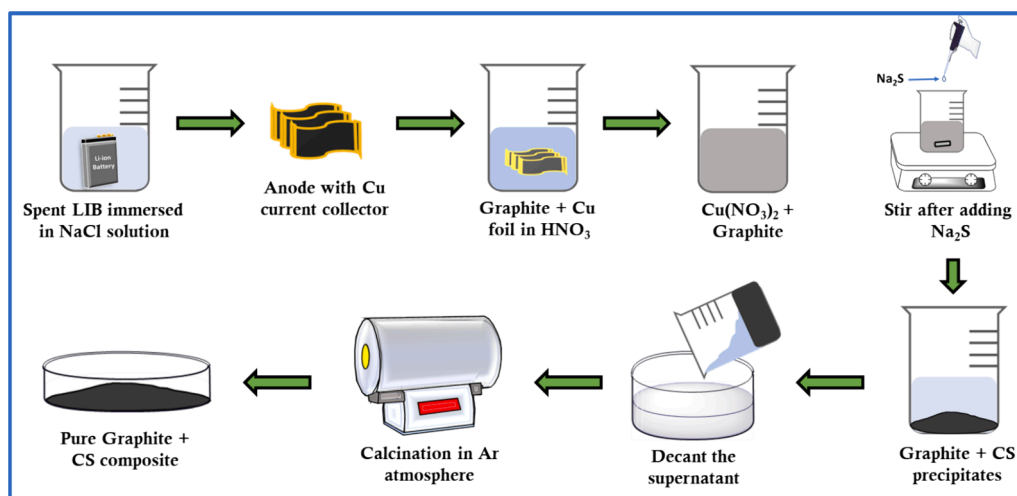
E-mail addresses: leey@chonnam.ac.kr (Y.-S. Lee), Aravind.van@gmail.com (V. Aravindan).

<https://doi.org/10.1016/j.cej.2024.155462>

Received 7 June 2024; Received in revised form 8 August 2024; Accepted 2 September 2024

Available online 3 September 2024

1385-8947/© 2024 Elsevier B.V. All rights are reserved, including those for text and data mining, AI training, and similar technologies.



Scheme 1. Flow chart of recovery/synthesis of RG-CS.

carbonaceous materials, conversion and alloying type metals, their oxides, and other Ti-based compounds, etc., are explored in NICs [10–15]. However, carbonaceous intercalation materials such as graphite and hard carbons are the most preferred anode because of their reversibility, stability, and excellent cycling performance. The other anode materials experience huge volume variation, thereby triggering the pulverization of electrodes, irreversibility, and cyclic instability, which results in poor electrochemical performances. It is well known that graphite is the most successful and unbeaten anode material in Li-ion batteries (LIBs) since Sony's commercialization in the early 1990s [16–18]. However, it was not considered a good choice as an anode for Na-based energy storage devices because of the thermodynamic instability of the binary graphite intercalation compound (*b*-GIC). Recently, a new concept called co-intercalation/solvated Na-ion intercalation has been found to form ternary GICs (*t*-GICs) in graphite electrodes. This reversible intercalation is stable and facile compared to the topotactic Li-ion intercalation process and subsequent formation of the *b*-GIC, LiC_6 [15,19–21]. This phenomenon completely depends on the solvent nature of the electrolyte and is a complex mechanism compared with the conventional metal-ion intercalation process into the graphitic layers.

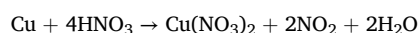
In this work, the anode material of spent LIBs is efficiently recovered and upcycled as the anode for NIC applications. Compared with the previous reports [22–24], we have directly used the spent electrode as an anode material in limited steps of recovery utilizing green aqueous solvents. Graphite is, as such, used after the thermal treatment, and the current collector, Cu-foil, is converted to copper sulphide (CuS). Hence, we obtained an anode material with CuS decoration on the graphite (RG-CS), translating to excellent electrochemical performance compared to previous works where pristine graphite was used as the anode. There are previous reports where they have recovered anodic material and current collectors to regenerate as anodes for Li/Na-ion batteries/capacitors. Natarajan *et al.* [22] treated the anode with acid to purify graphite and synthesize copper (II)-benzene 1,3,5 tricarboxylate (Cu-BTC MOF) from Cu-foil. These are used as the anodic materials for LIBs and NIBs. Akshay *et al.* [23,24] and Subramanyan *et al.* [25] recovered the spent LIB anode materials and current collectors separately, utilizing them as anodes for LIC and NIB, respectively. They used the recovered graphite directly as an anode, whereas the Cu-foil was transformed into CuO , making it a successful anodic material for both LIC and NIB. All the above reports separate the graphite and Cu-current collector before or after acid treatment. In the present work, we completely eliminate the separation step and the harmful organic solvent used for this process. Thus, recovered/synthesized RG-CS anodic material displayed superior electrochemical performance in both half/full-cell studies with better energy density, power density, and cyclic stability. The adaptability of the

NIC to various temperature conditions and its excellent performance are discussed in detail.

2. Experimental section

2.1. Regeneration of RG-CS from spent LIB anode

The spent/dead Lithium-ion batteries (LIBs) are collected from the local market and immersed in the NaCl solution overnight to discharge the batteries. The open circuit voltage (OCV) is checked for all the batteries, and the completely discharged ones are selected for safe dismantling. These batteries are cleaned using distilled water and dried in a hot air oven for about four hours. The dried batteries are safely dismantled inside the fume hood using cutters and pliers. Initially, the outer metal case is removed, and then the anode, cathode, and separator are separated. The anode is washed and dried, whereas the cathode and separator are stored for future recovery. The dried anode (graphite + Cu-foil) pieces were immersed in 15 ml conc. nitric acid (Sigma Aldrich, 69 %), resulting in the formation of bluish-green-coloured copper nitrate. The calculations are performed so that the copper nitrate formed is 1 molar. That is, the weight of copper foil + graphite in a unit square area of anode is determined, and further calculations are performed based on this. It is found that 7.15 g of anode consists of 2.54 g of Cu-foil and remaining graphite. So, the 7.15 g of the anode is immersed in 15 ml nitric acid, and the solution is made up to 40 ml by adding distilled water. The equation corresponding reaction is as follows:



To the copper nitrate solution, 10 ml of CTAB (hexadecyltrimethylammonium bromide, 0.1 M) surfactant was added and followed by 40 ml of sodium sulphide (Na_2S , 1 M) dropwise with constant stirring, resulting in the formation of copper sulphide (CS) precipitate. The graphite + CS composites in the solution were filtered out, dried, and heated at 650°C for 2 h in the argon atmosphere to get a pure-layered-graphite and copper sulphide composite. A detailed pictorial representation of the recovery/synthesis is given in Scheme 1.

2.2. Material characterisation

The powder X-ray diffraction (XRD) studies were performed using Rigaku Smartlab automated multipurpose X-ray diffractometer (40 kV, 200 mA, $\lambda = 1.5406 \text{ \AA}$) with $\text{Cu K}\alpha$ radiation to identify the phase and purity of the composite recovered/synthesized. The measurements were carried out for the sample from 10 to 80° at a scan rate of 1° min^{-1} . The Raman Spectroscopic studies were performed using the LabRam HR

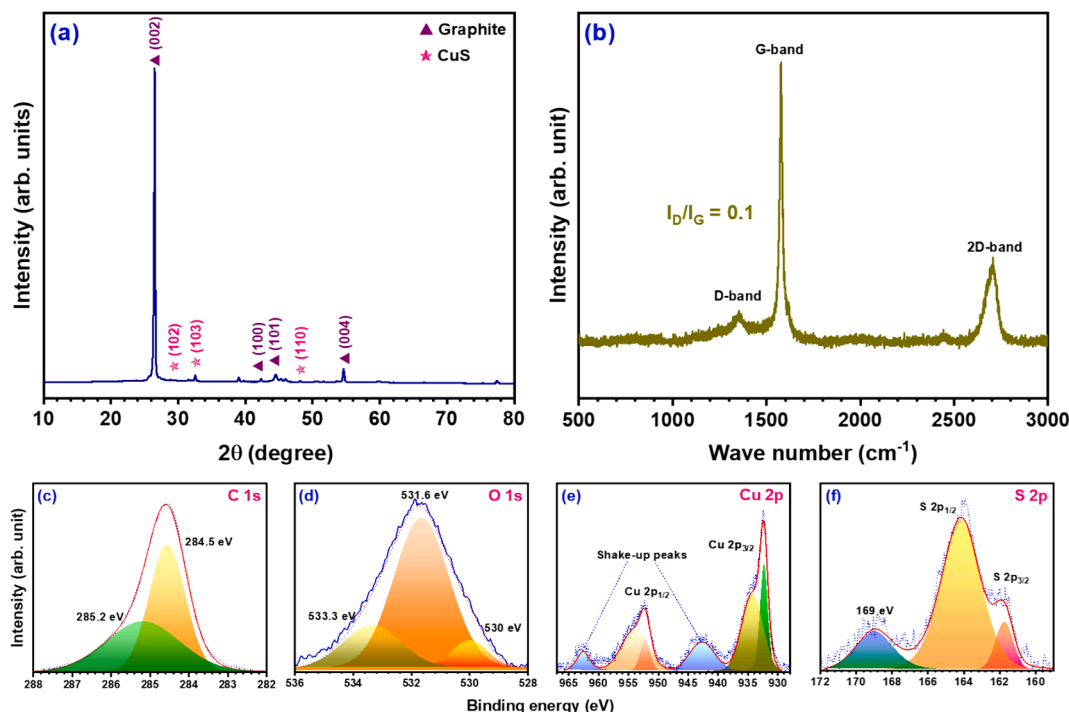


Fig. 1. Physical characterizations of RG-CS composite: (a) XRD pattern, (b) Raman spectra, and (c-f) deconvoluted XPS spectra.

Evolution Raman Spectrometer (Horiba Jobin-Yvon, France) with a 515 nm Diode laser as an excitation light source. The BET surface area, BJH pore size distribution, etc., were analysed using the automated gas sorption analyzer (Autosorb IQ-XR-XR-XR, 3 stat., Viton). Thermogravimetric analysis (TGA, Shimadzu, Japan) was performed in an air atmosphere to determine the thermal stability of the sample. Field emission scanning electron microscopy (FE-SEM, Gemini 560, Germany) and high-resolution transmission electron microscopy (HR-TEM, JEM-2000, EX-II, JEOL, Japan) analyzed the morphology and internal structure of the sample, respectively. The elemental composition of the sample was studied using energy-dispersive X-ray spectroscopy (EDS, Ametek).

2.3. Electrochemical characterization

All the electrochemical studies of the RG-CS composite were performed in half-cell and full-cell assemblies. Half-cells were fabricated with sodium as the reference/counter electrode and full cells with activated carbon (AC) as the counter electrode. First, the RG-CS samples were coated on Cu-foil to make the electrodes for the half-cell and full-cell assembly. The electrodes were prepared using the conventional slurry coating method in which the slurry consisted of 80% active material (RG-CS), 10% conductive carbon (acetylene black), and 10% of the binder (PVdF, polyvinylidene fluoride) in the N-methyl-2-pyrrolidone (NMP) solvent. The homogenous slurry is ready for the coating after stirring for more than 8 h. The slurry is thus coated over the Cu-foil at 13 mm thickness using the Doctor Blade apparatus (MSK-AFA-III Automatic Thick Film Coater, MTI Corporation). The uniform thin-coated RG-CS sample is rolled on a hot-roll press (Tester Sangyo, Japan) after completely drying in the hot air oven for a minimum of 4 h. In the final step of electrode preparation, the 12 mm diameter circular electrodes were punched out using the photographic electrode cutter to fabricate cells. The AC electrode (cathode in the full-cell assembly) was prepared by mixing the AC, acetylene black, and teflonized acetylene black (TAB-2) binder in a mortar pestle with ethanol as the solvent. A free-standing film of minimal thickness was prepared with proper mixing, and it was punched over the circular stainless-steel mesh (Goodfellow, UK) of 14

mm diameter using a hydraulic press (Specac, UK). It is then dried in the vacuum oven at 75 °C for more than 4 h before fabrication of cells.

All the cell fabrication was performed inside the glove box under the argon atmosphere with O_2 level <0.1 ppm and H_2O level <0.1 ppm. CR2016-type coin cells were employed for cell fabrication. The electrolyte was prepared by dissolving 1 M $NaCF_3SO_3$ (98%, Sigma Aldrich) salt in tetraethylene glycol dimethyl ether (TEGDME, >99%, Sigma Aldrich) solvent. The Whatman paper (1825-047, GF/F) separator ensured the physical separation between the anode and cathode. In the half-cell fabrication, sodium metal was the counter/reference electrode. For the full-cell fabrication, initially, the RG-CS electrode was paired with Na metal, and a half-cell was made. This is discharged/charged for a few cycles and terminated at the third discharge, forming a sodiated phase in graphite (Na^+ -solvent + graphite) and a conversion reaction in the copper sulfide ($CuS + 2Na \rightarrow Cu^0 + Na_2S$). The cell is then taken inside the glovebox and dismantled to take the pre-sodiated RG-CS electrode. It is then paired with the mass-balanced AC electrodes to form NIC, and further electrochemical studies were performed on this. The mass-balancing was performed by using the equation Eq. (1) (Supporting Information). All the electrochemical studies, including electrochemical impedance spectroscopy (EIS), cyclic voltammetry (CV), galvanostatic charge-discharge (GCD), etc., were performed using the Biologic BCS 805 (France) battery tester.

3. Results and discussion

3.1. Material characterization

The recovery and synthesis of the anodic material for our NIC were performed using simple steps without any harmful organic solvents such as dimethylformamide, N-methyl-2-pyrrolidone, etc. (Scheme 1). The purity and phase of the recycled/synthesized RG-CS composite were examined using the XRD measurement. The spectrum (Fig. 1a) consists of sharp peaks positioned at 26.5° corresponding to the 002 plane of graphite, a fingerprint reflection of graphite. This peak corresponds to the hexagonal crystal structure ($a = b = 2.46 \text{ \AA}$, $c = 6.71 \text{ \AA}$; $\alpha = \beta = 90^\circ$, and $\gamma = 120^\circ$) of graphite with 94: P63/*mmc* space group (DB card

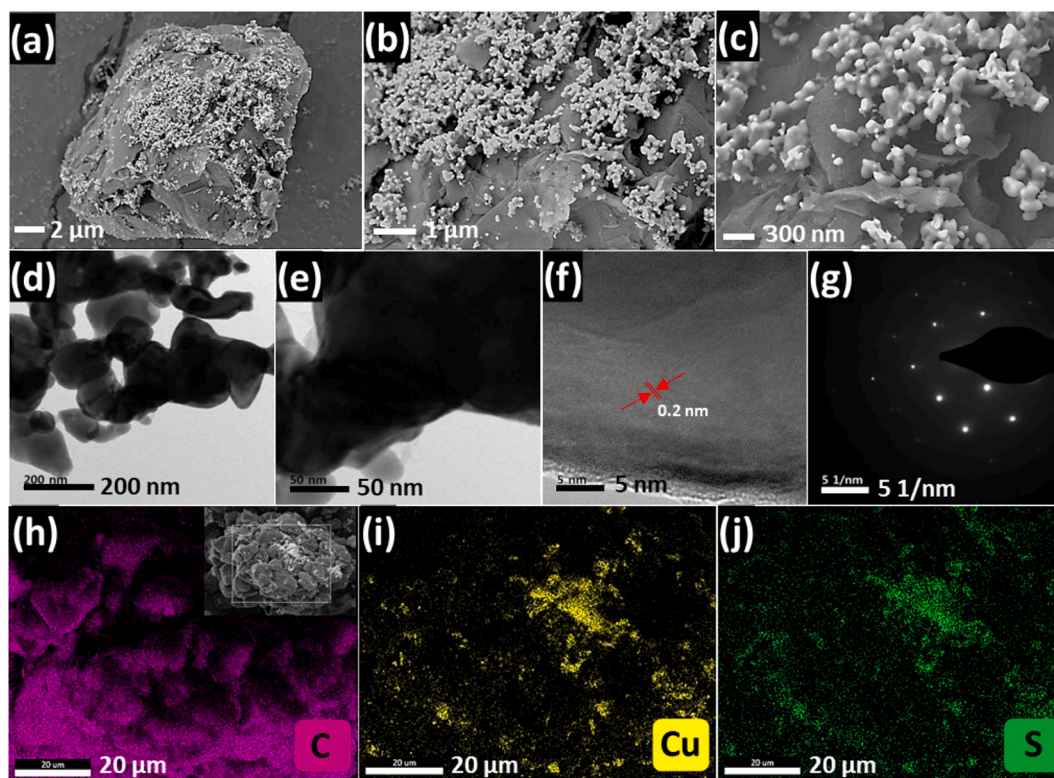


Fig. 2. Physical characterisations of RG-CS composite: (a-c) FE-SEM images at different magnifications, (d-f) TEM & HR-TEM images, (g) SAED pattern, and (h-j) EDS elemental mapping.

number: 9011577). The particle size of the sample was also calculated from the Debye–Scherrer equation (Eq. (2), given in the supplementary part) for the (002) peak and is found to be 34.4 nm. Further, the reflections observed at 44.5° and 54.6° indicate the graphite's (101) and (004) planes, respectively. We would also observe additional peaks apart from graphite, confirming the presence of CuS in trace amounts. The peaks located at 32° and 45.9° are of covellite phase (CuS) with (103) and (110) planes, respectively. The absence of other prominent peaks confirms the purity of the recycled/synthesized RG-CS composite.

The surface area and pore size distribution of the RG-CS composite were studied from the N_2 adsorption/desorption studies (Figure S1(a & b)). The composite exhibited a surface area of $12.6 \text{ m}^2/\text{g}$ with pore radius and pore volume around 14.8 \AA and 0.05 cc g^{-1} , respectively. Raman spectroscopic analysis was also performed for the sample in which the spectrum is given in Fig. 1b. Spectrum displays the characteristic peak at ~ 1353 , ~ 1576 , and $\sim 2706 \text{ cm}^{-1}$, corresponding to D, G, and 2D bands of the graphite, respectively. The D-band or dispersive/defect band corresponds to the structural imperfections in the graphite lattice, which usually occurs in the recycled graphite due to the unknown long cycling in LIB. The G-band or graphite band is a representative peak of graphite showing the in-plane stretching in sp^2 carbon of the hexagonal crystal structure. The 2D band corresponds to the second-order two-phonon process associated with the number of graphene layers in the graphite. The highly intense band also indicates the multilayer structure of the recycled/recovered graphite. The ratio of intensities of D-band (I_D) and G-band (I_G) is of great significance in determining the degree of disorder or graphitisation of the graphite. The higher the I_D/I_G ratio, the greater the disorderness. We calculated the ratio, which is found to be 0.1, confirming the more ordered structure of recycled/recovered graphite. In addition to the qualitative analysis of the carbon content from Raman spectroscopy, quantitative measurement of the carbon was performed using the thermogravimetric analysis (Figure S1(c)) and was found to be around 95% after thermal treatment. The chemical composition and the surface chemistry of the RG-CS

composite were studied using X-ray photoelectron spectroscopy (XPS). The XPS survey spectrum confirms the presence of only C, O, Cu, and S elements of the RG-CS composite, confirming the purity of the recovered sample. The deconvoluted C 1s and O 1s peaks are given in Fig. 1(c & d), and their positions are mentioned in the spectrum. The Cu 2p deconvoluted peaks at 932.3 and 934.3 eV correspond to Cu $2P_{3/2}$, and the peaks at 952.2 and 953.9 eV indicate the Cu $2P_{1/2}$ state. In addition, two peaks positioned at 942.7 and 962.6 eV, called satellite peaks, are formed due to the shake-up process during the electron excitation to the higher energy levels. The S 2P spectrum is deconvoluted to peaks positioned at 161.7 and 164.1 eV, indicating the S $2P_{3/2}$ and S $2P_{1/2}$ states, respectively. There is an additional peak at 169 eV corresponding to the covellite phases [26].

The surface morphology and structural characteristics of the RG-CS sample were studied using field emission-scanning electron microscopy (FE-SEM), transmission electron microscope (TEM), and high-resolution-transmission electron microscopic (HR-TEM) analysis. Fig. 2(a-c) displays the flaky nature of the graphite with the CS nanoparticles decorated over it. Though the graphite has undergone several cycles during the cycling and the recovery process, the morphology is not affected much, and the flaky nature is still intact. Fig. 2(d & e) displays the TEM images, and the HR-TEM image is shown in Fig. 2f. The interplanar distance of the graphite was also calculated and was found to be 2 nm. The crystalline nature of the RG and CS was further confirmed by the selected area electron diffraction (SAED) pattern and given in Fig. 2g. The EDS analysis once again confirms the presence of only C, Cu, and S elements (Fig. 2(h-j)). In addition to the XRD and XPS studies, the morphological analysis, i.e., EDS mapping confirms the purity of the recycled material.

3.2. Electrochemical studies

The electrochemical performance of the RG-CS sample was examined in the coin-cell assembly with Na-metal as the reference/counter

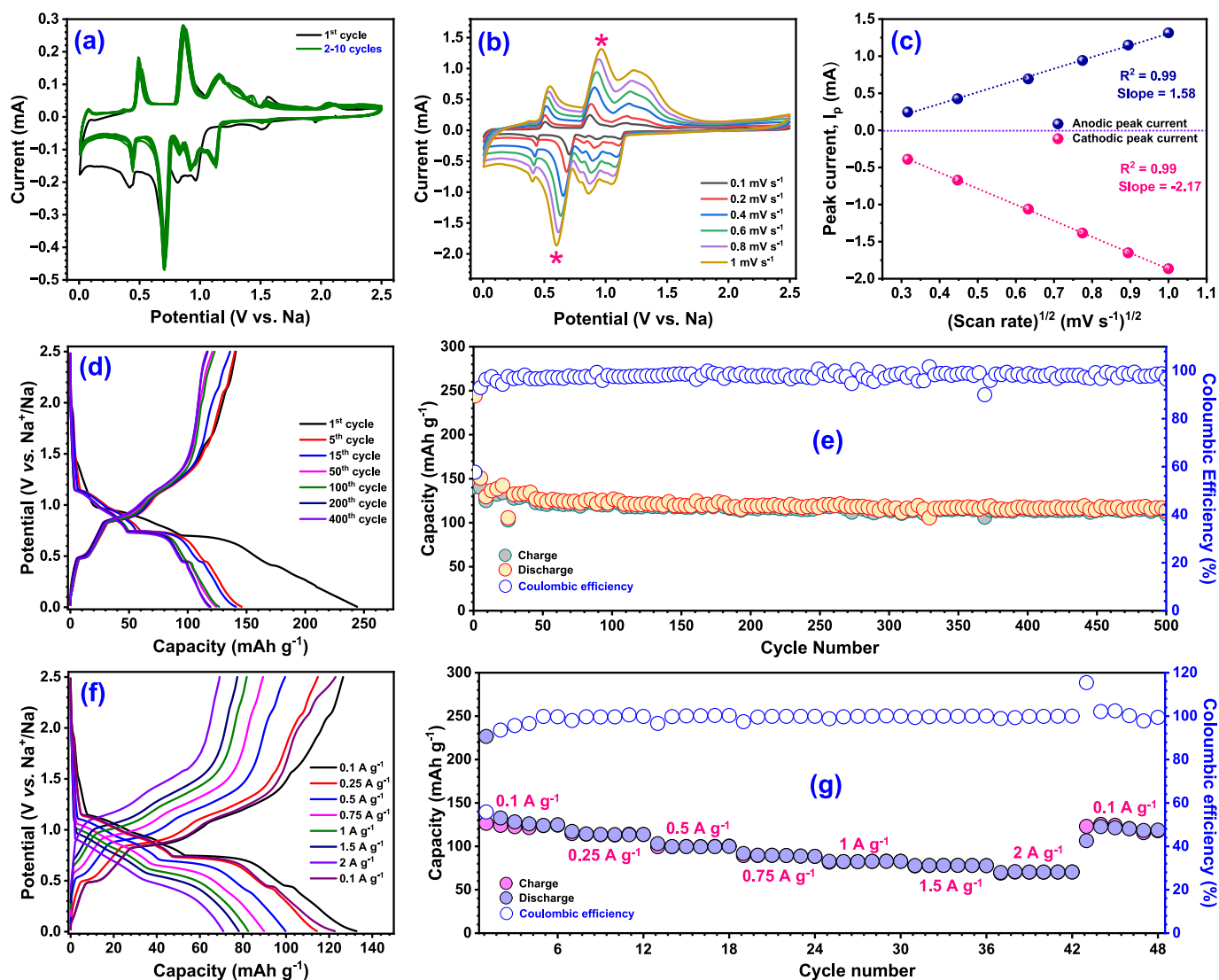


Fig. 3. Electrochemical performance of RG-CS half-cell configuration: (a) Cyclic voltammogram at scan rate of 0.1 mV s⁻¹, (b) CV at different scan rates (0.1 to 1 mV s⁻¹), (c) peak current vs. root of scan rate plot, (d) galvanostatic charge-discharge curves (1st, 5th, 15th, 50th, 100th, 200th, and 400th cycles) at a current density of 0.1 A g⁻¹, (e) capacity vs. cycle number plot, (f) galvanostatic charge-discharge curve at different current densities, and (g) rate performance at different current rates.

electrode and 1 M NaCF₃SO₃ in tetraethylene glycol dimethyl ether (TEGDME) as the electrolyte. Initially, the half-cell was subjected to CV studies in the potential window from 0.005 to 2.5 V vs. Na (Fig. 3a). The initial cathodic scan displays a sharp prominent peak at 0.69 V vs. Na and small peaks at 1.5, 0.96, 0.81, 0.42, and 0.005 V vs. Na. In the subsequent cycles and with the increase in the scan rate, only four cathodic peaks (0.96, 0.81, 0.69, and 0.42 V vs. Na) are prominent. These peaks indicate the co-intercalation process of Na⁺-solvent between graphitic layers by forming a complex *t*-GIC phase. The other peaks observed only in the first cycle correspond to the electrolyte decomposition/solid electrolyte interphase (SEI) layer formation. In the initial cycle during the anodic scan, two prominent sharp peaks at 0.48 and 0.86 V vs. Na, one broad peak at 1.15 V vs. Na, and a small peak at 1.56 V vs. Na are observed. After the first cycle, no significant change in the anodic and cathodic peaks is observed, except for the disappearance of a small peak cathodic peak positioned at 1.5 V vs. Na and an anodic peak at 1.56 V vs. Na. However, an increase in the peak current is observed after the first cycle. This could be due to the structural rearrangement of graphite, which eventually enhances the current, and this intensity is found to be constant for the subsequent cycles. So, we can infer that the initial rearrangement of graphitic layers enhanced the

structural stability, which is confirmed by the long-term cycling performance of the Na/RG-CS half-cell.

Fig. 3b displays the CV at different scan rates from 0.1 to 1 mV s⁻¹. It is observed that there is a negligible shift in the potential as the scan rate increases, which explains the high reversibility and less polarization of the cell. The diffusion coefficient was calculated from the Randles-Sevcik equation (Eq.(3), supplementary part) and obtained a value of 2.69×10^{-11} and 5.17×10^{-11} cm² s⁻¹ for anodic and cathodic peaks, respectively (Fig. 3c). The galvanostatic charge-discharge (GCD) of the RG-CS half-cell is given in Fig. 3d, which gives a promising result. It is observed that the charge-discharge plateaus of the half-cell agree with the CV results. The plateaus in the charge-discharge curve match well with the CV peaks. The cell delivered a discharge capacity of 244 mAh g⁻¹ with a lower coulombic efficiency of 57% in the first cycle, mainly due to the SEI layer formation. However, as the cycle progresses, the specific capacity becomes stable with a coulombic efficiency >97%. The cell displayed a stable specific capacity of 113 mAh g⁻¹ with a coulombic efficiency of >96% after 500 cycles (Fig. 3e). A comparative study was also performed on commercial graphite (CG) and recovered graphite (RG) to study the significance of CS decoration over RG, as illustrated in Figure S2. The Na/CG and Na/RG half-cells exhibited a specific capacity

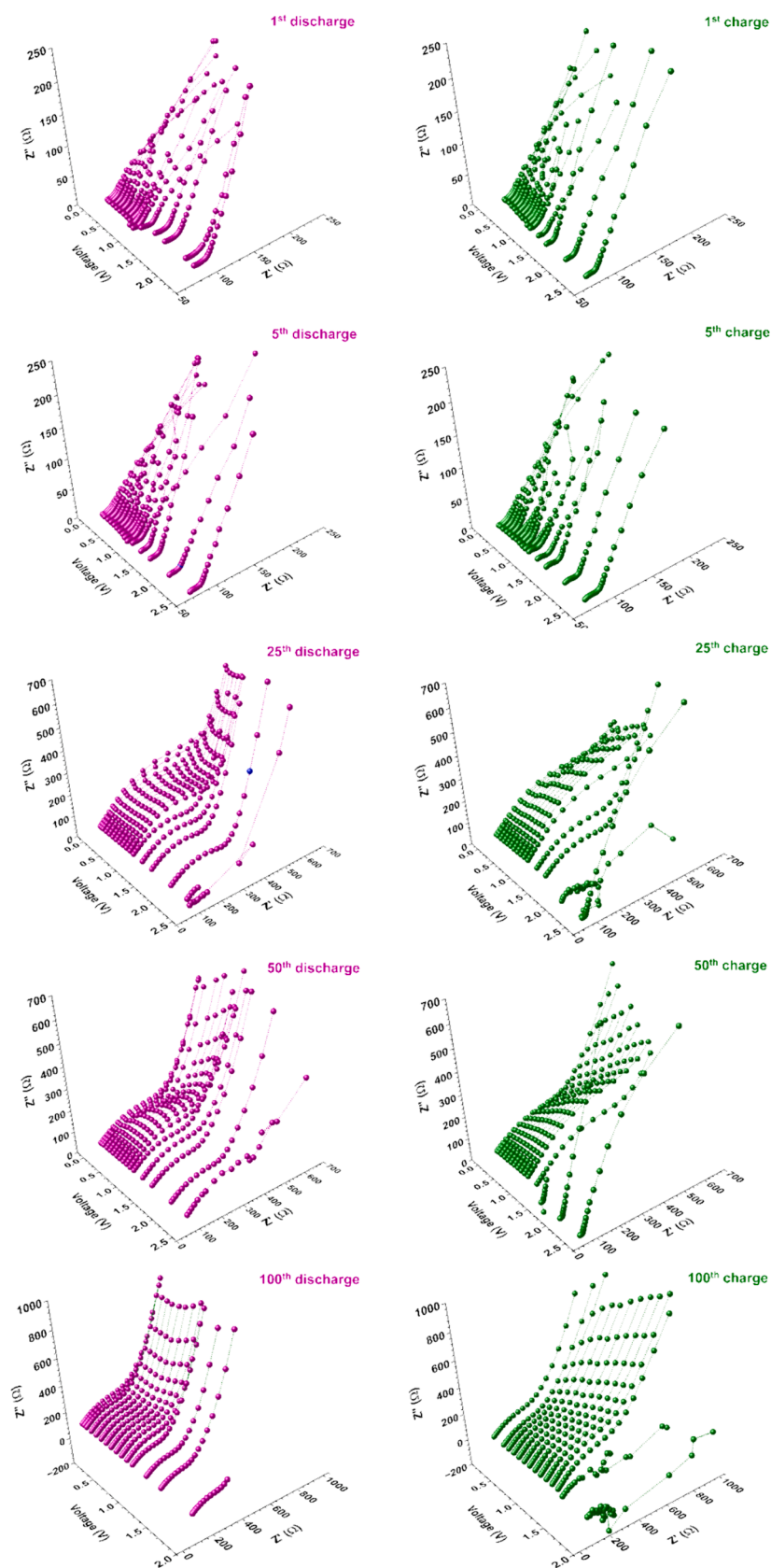


Fig. 4. *in-situ* electrochemical impedance spectroscopy (*in-situ*-EIS) profile of Na/RG-CS half-cell with traces of 1st, 5th, 25th, 50th, and 100th cycles at different potentials.

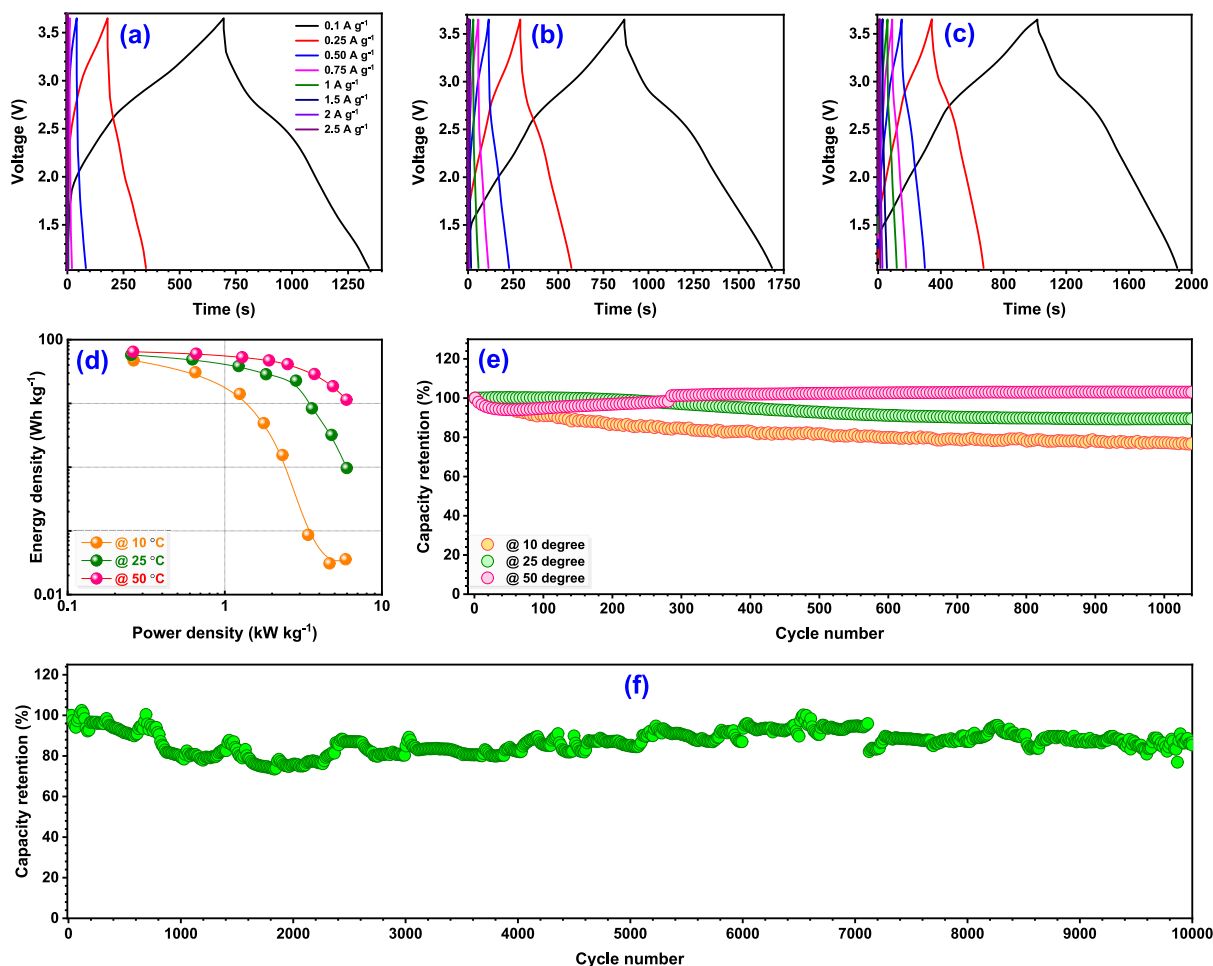


Fig. 5. Electrochemical performances of RG-CS//AC NIC: (a-c) E_{cell} vs. time graph at different temperatures (10, 25, and 50 $^{\circ}\text{C}$), (d) Ragone plot comparing energy and power density values at different temperatures, (e) long-term cycling profile at a current density of 0.75 A g^{-1} different temperatures, and (f) cycling profile at room temperature conditions at a current density of 0.75 A g^{-1} .

of 84 and 88 mAh g^{-1} , respectively, after 300 cycles, which is significantly lower than that of the RG-CS; hence, the superiority of RG-CS is confirmed and validated. Compared with previously reported works which utilise carbonaceous electrodes as the anode, the RG-CS performance was better in terms of capacity and cyclic stability. Divya *et al.* [27] utilised the RG from spent LIBs as anode for the NIC, where the half-cell exhibited $\sim 115 \text{ mAh g}^{-1}$ capacity at the lower current rate of 0.05 A g^{-1} . At the current density of 0.1 A g^{-1} , the capacity was further reduced to 90 mAh g^{-1} . Also, the same group explored the graphitic carbon nanofiber [10] as the anode, exhibiting a capacity of 118 mAh g^{-1} at lower current density of 0.05 A g^{-1} . The graphite composite from the pencil lead [28] was also used as an anode material but has a lower specific capacity of 114 mAh g^{-1} . Similarly, other works [15,29] with graphitic anode, too, have less specific capacity in half-cell compared with our anode. The Na/AC was also subjected to GCD in the potential window of 1.5 to 4.1 V vs. Na at a current density of 0.1 A g^{-1} . The cell displayed excellent cyclic stability for more than 100 cycles with a coulombic efficiency of $\sim 98\%$ (Figure S4).

The rate capability of the half-cell was examined by testing the cell at different current rates from 0.1 to 2 A g^{-1} and again switched back to 0.1 A g^{-1} (Fig. 3(f & g)). The cell displayed better rate performance at all the current densities. At lower current density, the cell has an average discharge capacity of 127 mAh g^{-1} . As the current density progresses, a slight drop in specific capacity is observed, which is a common phenomenon. However, when the current density is reduced to 0.1 A g^{-1} again, $>95\%$ of the initial capacity is retained, which indicates the

stability and reversibility of the RG-CS. The comparative rate performance study between RG-CS, CG and CuS is given in the supplementary section (Figure S3).

The SEI layer is an important component of the cell that determines electrochemical performance. The robust SEI enhances the reversibility, stability, and overall performance of the cell. Therefore, continuous *in-situ*-electrochemical impedance spectroscopy (*in-situ*-EIS) analysis was performed for the Na/RG-CS half-cell, where the impedance was recorded at different potentials of the voltage window. Fig. 4 displays the representative traces of the 1st, 5th, 25th, 50th, and 100th cycles of the continuous analysis. The initial discharge has an increased charge transfer resistance (R_{CT}) because of the electrolyte decomposition and the following SEI layer formation. However, as the cycle progresses, the R_{CT} value is reduced and stable, which can be observed in the 5th cycle. After 25 cycles, a slight increase in the R_{CT} value is observed, which may be because of the volume variation or the structural rearrangement of the RG-CS. But this value is found to be stable till the 100th cycle of charge-discharge, which confirms the robustness and stability of the structure and the SEI layer formed.

The NICs are hybrid devices that involve different energy storage mechanisms (electrochemically and electrostatically) in anode and cathode. The battery-type anode stores energy through the faradaic reaction, whereas the capacitive-type cathode utilizes the non-faradaic adsorption/desorption process for charge storage. Because of the different charge storage mechanisms, a kinetic mismatch occurs between the anode and cathode, which may result in poor NIC

performance. This mismatch can be equalized by balancing the charge (called mass-balancing) on both sides (anodic and cathodic) of the electrodes used in NIC (Eq. (1), supplementary part). So, mass-balancing is a significant step to realize high-performance NICs. Initially, the Na/RG-CS half-cell is fabricated, subjected to charge–discharge for a few cycles, and terminated at the 3rd discharge. This forms the sodiated phase in graphite and the conversion reaction in the copper sulfide as well ($\text{CuS} + 2\text{Na} \rightarrow \text{Cu}^0 + \text{Na}_2\text{S}$). The cell is then dismantled inside the glove box, and the electrode is subsequently paired with the mass-balanced AC to form RG-CS//AC full cell. The NIC was subjected to galvanostatic charge–discharge studies at various current rates and different temperature conditions. Fig. 5(a–c) displays the E_{cell} vs. time graphs of the full-cell at different temperature conditions (0, 25, and 50 °C). We could observe a slight drop in the potential due to the resistance offered by the components of the NIC, which is called the ohmic drop or ohmic polarisation or IR drop (ΔE_{ohm}). Figure S5 displays the plot of ohmic drop vs. applied current density at different temperatures, which shows the increase in the ohmic drop with the rise in the current density. The elevation in temperature increases the conductivity of the cell and thereby reduces the ΔE_{ohm} value, which can also be observed from the graph. The Ragone plot in Fig. 5d represents the energy density and power density values of the NIC at different current rates and temperatures. The energy and power density (equation for calculation of energy/power density is given in supplementary part, Eq. (4)) values of the NIC were calculated based on the total active material loading in both anode and cathodes (2.48 mg and 4.18 mg, respectively). Accordingly, the NIC delivered maximum energy/power densities of 64.6 Wh kg^{−1}/5.9 kW kg^{−1}, respectively. We did a comparative study (figure S6) with previously reported works to understand where our NIC stands in terms of energy/power density values. Further, the full-cell was also subjected to long-term cycling at different temperature conditions, and the excellent capacity retention of ≥90% after 1000 cycles was observed at 25 and 50 °C (Fig. 5e). In addition to the temperature study, the long-term cyclic study was performed at a higher current rate of 0.75 A g^{−1} at room temperature conditions as shown in Fig. 5f. The NIC was cycled for more than 10,000 cycles, and we could observe excellent capacity retention of >85%, which is above the benchmark for practical applications. Besides the active materials harvested from the dead LIBs, we strongly believe that the excellent performance of NIC is mainly because of the efficient utilization of both the solvent-co-intercalation process and conversion mechanism (to a small extent), balancing active materials in both electrodes and a suitable testing window.

4. Conclusion

In this work, we have successfully upcycled the anode (graphite + Cu-foil current collector) of spent LIBs into anode material (RG-CS) for the NIC applications. Simple, green, and economical ways of recovery and synthesis were employed for the generation of a new combination anode. Na-storage properties were evaluated from the half-cell studies by pairing the active material with sodium metal, and different electrochemical studies were performed. The RG-CS displayed excellent cyclic stability of more than 500 cycles with superior capacity and coulombic efficiency. The interfacial properties of the Na/RG-CS were analyzed from the *in-situ*-impedance studies, which validate the stability/robustness of the SEI layer form. The RG-CS//AC-based NIC displayed a superior energy density and power density of 64.6 Wh kg^{−1} and 5.9 kW kg^{−1}, respectively, at ambient temperature conditions. The long-term cycling performance at room temperature was mesmerizing as it retained >85% of the capacity after 10,000 charge–discharge cycles. The possibility of NIC at different temperatures was studied, where the full-cell displayed better performance at all the temperature conditions. Overall, the performance of the RG-CS//AC NIC was remarkable, and further research is being done to enhance the electrochemical performance. This study clearly shows that an efficient upcycling of the dead

LIBs not only serves as a source of high-performance active materials for charge storage devices but also keeps the environment clean and tidy.

Declaration of competing interest

The authors declare that they have no known competing financial interests or personal relationships that could have appeared to influence the work reported in this paper.

Data availability

Data will be made available on request.

Acknowledgement

SJ thanks the Prime Minister's Research Fellowship (0902009) for financial support. YSL acknowledges the financial support from the National Research Foundation of Korea (NRF) grant funded by the Korean government (Ministry of Science, ICT&Future Planning) (No. RS-2023-00208361). V.A. acknowledges financial support from the Anusandhan National Research Foundation (ANRF), Govt. of India, through Swarnajayanti Fellowship (SB/SJF/2020-21/12) and Core Research Grant (CRG/2023/000013).

Appendix A. Supplementary data

Supplementary data to this article can be found online at <https://doi.org/10.1016/j.cej.2024.155462>.

References

- [1] J. Xie, Y.-C. Lu, A Retrospective on Lithium-Ion Batteries, *Nat. Commun.* 11 (1) (2020) 2499, <https://doi.org/10.1038/s41467-020-16259-9>.
- [2] M. Li, J. Lu, Z. Chen, K. Amine, 30 Years of Lithium-Ion Batteries, *Adv. Mater.* 30 (33) (2018) 1800561, <https://doi.org/10.1002/adma.201800561>.
- [3] W. Zuo, R. Li, C. Zhou, Y. Li, J. Xia, J. Liu, Battery-supercapacitor hybrid devices: recent progress and future prospects, *Adv. Sci. (Weinheim, Baden-Württemberg, Ger.)* 4 (7) (2017), <https://doi.org/10.1002/advs.201600539>.
- [4] A. Muzaffar, M.B. Ahamed, K. Deshmukh, J. Thirumalai, A Review on Recent Advances in Hybrid Supercapacitors: Design, Fabrication and Applications, *Renew. Sustain. Energy Rev.* 101 (2019) 123–145, <https://doi.org/10.1016/j.rser.2018.10.026>.
- [5] S. Jayaraman, A. Jain, M. Ulaganathan, E. Edison, M.P. Srinivasan, R. Balasubramanian, V. Aravindan, S. Madhavi, Li-Ion vs. Na-Ion Capacitors: A Performance Evaluation with Coconut Shell Derived Mesoporous Carbon and Natural Plant Based Hard Carbon, *Chem. Eng. J.* 316 (2017) 506–513, <https://doi.org/10.1016/j.cej.2017.01.108>.
- [6] V. Aravindan, M. Ulaganathan, S. Madhavi, Research Progress in Na-Ion Capacitors, *J. Mater. Chem. A* 4 (20) (2016) 7538–7548, <https://doi.org/10.1039/c6ta02478e>.
- [7] P. Cai, K. Zou, X. Deng, B. Wang, M. Zheng, L. Li, H. Hou, G. Zou, X. Ji, Comprehensive Understanding of Sodium-Ion Capacitors: Definition, Mechanisms, Configurations, Materials, Key Technologies, and Future Developments, *Adv. Energy Mater.* 11 (16) (2021) 2003804, <https://doi.org/10.1002/aenm.202003804>.
- [8] Z. Zhang, Z. Gu, C. Zhang, J. Li, C. Wang, Sodium-Ion Capacitors: Recent Development in Electrode Materials, *Batter. & Supercaps* 4 (11) (2021) 1680–1700, <https://doi.org/10.1002/batt.202100042>.
- [9] R. Thangavel, B.K. Ganesan, V. Thangavel, W.-S. Yoon, Y.-S. Lee, Emerging Materials for Sodium-Ion Hybrid Capacitors: A Brief Review, *ACS Appl. Energy Mater.* 4 (12) (2021) 13376–13394, <https://doi.org/10.1021/acsaelm.1c02099>.
- [10] M.L. Divya, S. Jayaraman, Y.S. Lee, V. Aravindan, High Energy Na-Ion Capacitor Employing Graphitic Carbon Fibers from Waste Rubber with Diglyme-Based Electrolyte, *Chem. Eng. J.* 426 (June) (2021) 130892, <https://doi.org/10.1016/j.cej.2021.130892>.
- [11] A. Chaturvedi, P. Hu, Y. Long, C. Kloc, S. Madhavi, V. Aravindan, High Power Na-Ion Capacitor with TiS₂ as Insertion Host, *Scr. Mater.* 161 (2019) 54–57, <https://doi.org/10.1016/j.scriptamat.2018.10.016>.
- [12] W. Zhang, F. Zhang, F. Ming, H.N. Alshareef, Sodium-Ion Battery Anodes: Status and Future Trends, *EnergyChem* 1 (2) (2019) 100012, <https://doi.org/10.1016/j.enchem.2019.100012>.
- [13] L. Fang, N. Bahlawane, W. Sun, H. Pan, B. Xu, M. Yan, Y. Jiang, Conversion-Alloying Anode Materials for Sodium Ion Batteries, *Small* 17 (37) (2021) 2101137, <https://doi.org/10.1002/smll.202101137>.
- [14] J. Wang, Z. Li, S. Ramesh, S.B. Aziz, D. Zhang, H. Jiunn Woo, Q. Wang, B. Wang, Recent Advances in Metal Oxides for Sodium-Ion Capacitors: Mechanism,

- Materials, and Future Prospects, *Chem. Eng. J.* 478 (2023) 147485, <https://doi.org/10.1016/j.cej.2023.147485>.
- [15] Z.-L. Xu, G. Yoon, K.-Y. Park, H. Park, O. Tamwattana, S. Joo Kim, W.M. Seong, K. Kang, Tailoring Sodium Intercalation in Graphite for High Energy and Power Sodium Ion Batteries, *Nat. Commun.* 10 (1) (2019) 2598, <https://doi.org/10.1038/s41467-019-10551-z>.
- [16] Y. Wen, K. He, Y. Zhu, F. Han, Y. Xu, I. Matsuda, Y. Ishii, J. Cumings, C. Wang, Expanded Graphite as Superior Anode for Sodium-Ion Batteries, *Nat. Commun.* 5 (May) (2014) 1–10, <https://doi.org/10.1038/ncomms5033>.
- [17] G. Ávall, M. Goktas, P. Adelhelm, Graphite as an Anode Material in Sodium-Ion Batteries, in: *Sodium-Ion Batteries*, John Wiley & Sons Ltd, 2022, pp. 1–25, <https://doi.org/10.1002/9783527825769.ch1>.
- [18] J. Asenbauer, T. Eisenmann, M. Kuenzel, A. Kazzazi, Z. Chen, D. Bresser, The Success Story of Graphite as a Lithium-Ion Anode Material-Fundamentals, Remaining Challenges, and Recent Developments Including Silicon (Oxide) Composites, *Sustain. Energy Fuels* 4 (11) (2020) 5387–5416, <https://doi.org/10.1039/d0se00175a>.
- [19] M.L. Divya, Y.-S. Lee, V. Aravindan, Solvent Co-Intercalation: An Emerging Mechanism in Li-, Na-, and K-Ion Capacitors, *ACS Energy Lett.* 6 (12) (2021) 4228–4244, <https://doi.org/10.1021/acsenergylett.1c01801>.
- [20] J. Xu, Y. Dou, Z. Wei, J. Ma, Y. Deng, Y. Li, H. Liu, S. Dou, Recent Progress in Graphite Intercalation Compounds for Rechargeable Metal (Li, Na, K, Al)-Ion Batteries, *Adv. Sci.* 4 (10) (2017) 1700146, <https://doi.org/10.1002/advs.201700146>.
- [21] P. Han, X. Han, J. Yao, L. Zhang, X. Cao, C. Huang, G. Cui, High Energy Density Sodium-Ion Capacitors through Co-Intercalation Mechanism in Diglyme-Based Electrolyte System, *J. Power Sources* 297 (2015) 457–463, <https://doi.org/10.1016/j.jpowsour.2015.08.011>.
- [22] S. Natarajan, R.M. Bhattarai, M.S.P. Sudhakaran, Y.S. Mok, S.J. Kim, Recycling of Spent Graphite and Copper Current Collector for Lithium-Ion and Sodium-Ion Batteries, *J. Power Sources* 577 (March) (2023) 233170, <https://doi.org/10.1016/j.jpowsour.2023.233170>.
- [23] M. Akshay, K. Subramanyan, Y.-S. Lee, V. Aravindan, An Order Magnitude Increase in Energy of Li-Ion Capacitors by Adopting Combined Insertion-Conversion Process with Long Durability and Water Soluble Binder, *Sustain. Mater. Technol.* 36 (2023) e00603.
- [24] M. Akshay, K. Subramanyan, M.L. Divya, Y.-S. Lee, V. Aravindan, Choice of Binder on Conversion Type CuO Nanoparticles toward Building High Energy Li-Ion Capacitors: An Approach Beyond Intercalation, *Adv. Mater. Technol.* 7 (9) (2022) 2200423, <https://doi.org/10.1002/admt.202200423>.
- [25] K. Subramanyan, M. Akshay, Y.S. Lee, V. Aravindan, Na-Ion Battery with Graphite Anode and Na₃V₂(PO₄)₃ Cathode via Solvent-Co-Intercalation Process, *Adv. Mater. Technol.* 7 (12) (2022) 1–7, <https://doi.org/10.1002/admt.202200399>.
- [26] N. Karikalan, R. Karthik, S.M. Chen, C. Karupiah, A. Elangovan, Sonochemical Synthesis of Sulfur Doped Reduced Graphene Oxide Supported CuS Nanoparticles for the Non-Enzymatic Glucose Sensor Applications, *Sci. Rep.* 7 (1) (2017) 1–10, <https://doi.org/10.1038/s41598-017-02479-5>.
- [27] M.L. Divya, S. Natarajan, Y.S. Lee, V. Aravindan, Highly Reversible Na-Intercalation into Graphite Recovered from Spent Li-Ion Batteries for High-Energy Na-Ion Capacitor, *ChemSusChem* 13 (21) (2020) 5654–5663, <https://doi.org/10.1002/cssc.202001355>.
- [28] M.L. Divya, Y.S. Lee, V. Aravindan, Glyme Solvated Na and Li-Ion Capacitors Based on Co-Intercalation Process Using Pencil Graphite as Battery Type Electrode, *J. Power Sources* 543 (May) (2022) 231823, <https://doi.org/10.1016/j.jpowsour.2022.231823>.
- [29] M. Goktas, C. Bolli, E.J. Berg, P. Novák, K. Pollok, F. Langenhorst, M.V. Roeder, O. Lenchuk, D. Mollenhauer, P. Adelhelm, Graphite as Cointercalation Electrode for Sodium-Ion Batteries: Electrode Dynamics and the Missing Solid Electrolyte Interphase (SEI), *Adv. Energy Mater.* 8 (16) (2018) 1–11, <https://doi.org/10.1002/aenm.201702724>.